JOURNAL OF AIRCRAFT
Vol. 47, No. 1, January–February 2010

Toward Real-Time Aero-Icing Simulation of Complete Aircraft via FENSAP-ICE

Kunio Nakakita,* Siva Nadarajah,† and Wagdi Habashi‡
McGill University, Montreal, Quebec H3A 2S6, Canada

DOI: 10.2514/1.44077

Three-dimensional fully viscous turbulent aero-icing flow simulation remains too computationally intensive when broad parametric studies are needed, such as during a certification process. In addition, the introduction of realistic icing effects for training pilots in simulators clearly lags behind in terms of taking advantage of computational fluid dynamics. To make such simulations more practical, this work presents a reduced-order modeling, based on the proper orthogonal decomposition method, that predicts a wide swath of approximate flowfields and ice shapes based on a limited number of "snapshots" obtained from high-fidelity computations. Modes are extracted from these snapshots and used to reconstruct the computational fluid dynamics field, and/or the aerodynamic coefficients, and/or the ice shapes for other conditions within the range. This reduces calculation times by two to three orders of magnitude from the full three-dimensional ones, enabling a more complete map of the performance of an iced aircraft over a wide range of flight and weather conditions to be used in its certification and pilot training.

Nomenclature

C_D = drag coefficient
C_{ice} = specific heat for ice
C_w = specific heat for water
Fr = Froude number
$\mathbf{g}$ = gravity vector
h_f = water film thickness, m
$J[\psi]$ = maximization problem as a function of ψ
K = inertia parameter
L_{evap} = latent heat of evaporation
L_{fusion} = latent heat of fusion at 0°C
L_{subl} = latent heat of sublimation
$\dot{m}_{\text{evap}}$ = mass flux of entering water lost due to evaporation or sublimation, $\text{kg}/(\text{m}^2\,\text{s})$
$\dot{m}_{\text{ice}}$ = mass flux of water lost due to ice accretion, $\text{kg}/(\text{m}^2\,\text{s})$
$\dot{Q}_h$ = convective heat flux
Re = Reynolds number
Re_d = droplet Reynolds number, $\frac{\rho d U_\infty |\mathbf{V}_a - \mathbf{V}_d|}{\mu}$
$R_{i,j}$ = autocorrelation matrix corresponding to i and j
T = temperature, K
$\tilde{T}_{d,\infty}$ = droplet temperature, C
U^i = ith snapshot data
$\mathbf{u}_a$ = air velocity
$\mathbf{u}_d$ = droplet impact velocity
x^i = value of the ith first variable
y^i = value of the ith second variable
α = coefficient of the basis function (proper orthogonal decomposition calculation), water volume fraction (for droplet calculation), angle of attack
β = total collection efficiency
ε = emissivity
λ = eigenvalues
μ = dynamic viscosity, $\text{kg}/(\text{s}\,\text{m})$
ρ_a = air density, kg/m^3
ρ_d = droplet density, kg/m^3
ρ_w = water density, kg/m^3
σ = Boltzmann constant
ψ = basis function (vector) of the proper orthogonal decomposition construction
Ω = spatial domain
ϖ = eigenvectors

Subscripts

w = water
$*$ = dimensionless number
∞ = freestream condition

I. Introduction

THERE are some significant limitations that still exist today in terms of certifying an aircraft to fly into known icing and in honing pilot skills in situations of ice accretion during flight. First, in terms of certification, although simulation (taken to mean all methods other than natural flight testing) is an acceptable means of compliance, computational fluid dynamics (CFD) is at the low end of the totem pole compared to using icing tunnels or flying behind icing tankers. Although CFD-based three-dimensional icing simulation codes can now handle increasingly complex icing physics and aircraft geometries, only a limited number of such runs may be afforded because of the length of time they take. Because only simplified or truncated geometries can be placed in a tunnel, and not all icing conditions can be reproduced in a tunnel or behind a tanker, there is no possibility of exploring the entire combined icing and aircraft-specific aerodynamic envelope via simulation unless drastic reductions in CFD computing time are achieved.

A second aspect is that pilots are almost unanimous in that their training on iced aircraft behavior is rudimentary. In a simulator, ice increases weight and shifts the center of gravity. In actual flight, different types of ice, at different temperatures and rates of accretion, coupled with the flight characteristics of the specific aircraft, can have dramatically different effects [1]. Some aircraft are known to be

---

Presented as Paper 4281 at the 25th AIAA Applied Aerodynamics Conference, Miami, FL, 25–28 June 2007; received 28 February 2009; revision received 13 July 2009; accepted for publication 14 July 2009.

*Masters Student, Multidisciplinary Computational Fluid Dynamics Laboratory, Department of Mechanical Engineering, 688 Sherbrooke Street West; currently Aircraft Engine R&D Center, Honda R&D Company, Ltd., Saitama, Japan. Member AIAA.

†Associate Professor, Multidisciplinary Computational Fluid Dynamics Laboratory, Department of Mechanical Engineering, 688 Sherbrooke Street West. Member AIAA.

‡Professor and Director, NSERC-J. Armand Bombardier Industrial Research Chair, Multidisciplinary Computational Fluid Dynamics Laboratory, Department of Mechanical Engineering, 688 Sherbrooke Street West. Associate Fellow AIAA.

so ice sturdy that almost no amount of ice can affect them, whereas others can, at the first sign of roughness caused by ice, exhibit sluggish or dangerous behavior. This, coupled with the fact that effective ice detection sensors are still considered a "work in progress," makes training with a higher-fidelity simulator an important need. Thus, it may be time to bring to bear on simulators some of CFD's successes in the prediction of aircraft-specific performance degradation. The enormous difficulty, again, would be to carry out a sufficiently significant number of such calculations to populate a look-up database or, eventually, to respond to pilot maneuvers in real time.

To inch toward a practical solution to these two problems, we introduce reduced-order models (ROMs) to rapidly predict flows and ice shapes for three-dimensional viscous turbulent flows over full aircraft configurations. Detailed CFD and icing calculations of sample points (snapshots) within the combined aerodynamic and icing environment envelope are performed via FENSAP-ICE, a high-fidelity three-dimensional code solving the Reynolds averaged Navier–Stokes (RANS) equations along with transport equations for the collection efficiency and ice formation/shapes. The proper orthogonal decomposition (POD) approach is then shown to be an effective ROM to rapidly reconstruct the flow and/or the ice shapes for other flight conditions within the set of snapshots computed by FENSAP-ICE.

II. Theory

A. Low-Fidelity and High-Fidelity Models of Icing

Numerical simulation is crucial in providing solutions to many areas of in-flight icing research: anti-icing and de-icing systems power requirements; performance degradation due to ice, pilot training, etc. However, the current slew of computational software for aero-icing is either based on low-fidelity models that are inapplicable to complex geometries or high-fidelity models that may be too costly for broad parametric studies of such systems. In both cases, low- and high-fidelity simulations, none is amenable to real-time or even nearly real-time simulation. Traditionally, low-fidelity models would either sacrifice geometric fidelity by using a 2-D assumption to tackle the problem section by section (say airfoils) and stack them to represent a complete aerodynamic entity (say a wing) or sacrifice physical modeling by using an inviscid and/or an incompressible assumption. Although the attraction of low-fidelity models is their low computational cost and fast turnaround, they are not able to provide meaningful solutions to most 3-D icing cases of interest as they are in a more difficult regime than trim cruise flight or for rotating flows such as in multistage jet engines or with helicopter rotors and blades.

In the present work, the high-fidelity model is that of FENSAP-ICE, a fully 3-D ice accretion system demonstrated for complex geometries and consisting of a suite of modules (FENSAP [2], DROP3D [3], and ICE3D [4]) that successively solve for flow, collection efficiency, and ice shapes, based on Eulerian models and RANS equations. The models have been extensively validated in [2,4] and their individual numerical precision, mesh independence, and closeness to experimental values have been well documented in the aforementioned references and will not be expanded on here.

FENSAP solves the Reynolds averaged Navier–Stokes equations by a finite element method (FEM) for the spatial discretization, and the equation is linearized by a Newton method. The one-equation Spalart–Allmaras [5] model provides the turbulent viscosity. To advance the solution in time, an implicit Gear scheme is used, along with a generalized minimal residual method procedure to iteratively solve the resulting matrix system. Quite important for ice-shape accuracy, heat fluxes at the walls are calculated via a consistent FEM approach [6].

DROP3D is a fully 3-D (as opposed to quasi-3-D) Eulerian approach [3] for airflows containing water droplets. Suitable variables (water volume fraction and droplet velocity) are computed at the same nodes of the discretized domain where the airflow variables have already been determined, and no particles have to be tracked through the mesh as in the traditional Lagrangian approach for droplets' trajectories. The Eulerian mode is a two-fluid approach consisting of the Navier–Stokes equations for dry air, augmented by the following water volume fraction-related continuity and momentum equations:

$$\frac{\partial \alpha}{\partial t} + \nabla \cdot (\alpha \mathbf{u}_d) = 0 \tag{1}$$

$$\frac{\partial \mathbf{u}_d}{\partial t} + \mathbf{u}_d \cdot \nabla \mathbf{u}_d = \frac{C_D Re_d}{24K}(\mathbf{u}_a - \mathbf{u}_d) + \left(1 - \frac{\rho_a}{\rho_w}\right)\frac{1}{Fr^2}\mathbf{g} \tag{2}$$

The drag coefficient for the spherical droplets is based on empirical formulations [7]. The droplets' velocity, as well as the liquid water content, is imposed at freestream. The droplet velocity is set to zero on the walls at the beginning of the iteration. The FEM is used to discretize the equations, with a streamline upwinding Petrov–Galerkin stabilization term [8] added.

ICE3D is a 3-D module used to compute ice accretion using the frictional forces and heat fluxes from the viscous flow solution provided by FENSAP and the water volume fraction provided by DROP3D. The partial differential equations are derived from the classical Messinger model [9]. The formulation starts with the assumption that the velocity profile, $\mathbf{u}(\mathbf{x}, y)$, for the water film is defined as follows:

$$\mathbf{u}(\mathbf{x}, y) = \left(\frac{\tau_{\text{wall}}}{\mu_w} - \frac{h_f}{\mu_w}\frac{\mathrm{d}p}{\mathrm{d}s}\right) y(\mathbf{x}) \tag{3}$$

where τ_{wall}, the shear stress from the air, is the main driving force for the water film; the pressure force is negligible except close to the stagnation point and the velocity is zero at the wall. For very thin films, the terms of order higher than one in the velocity profile are negligible; therefore, the velocity profile within the water film takes on a linear profile. In icing or anti-icing simulations, water film thicknesses are seldom above 10 μm [10] and a constant average temperature can be assumed through the water film. These assumptions result in a system of partial differential equations, for which the conservation of mass of the water film imposes

$$\rho_w \left[\frac{\partial h_f}{\partial t} + \mathrm{div}(\bar{\mathbf{u}} h_f)\right] = U_\infty \mathrm{LWC}\beta - \dot{m}_{\text{evap}} - \dot{m}_{\text{ice}} \tag{4}$$

where the three terms on the right-hand side correspond to the mass transfer by water droplet impingement (source for the film), the evaporation, and the ice accretion (sinks for the film), respectively. The conservation of energy equation can be formulated as

$$\begin{aligned} &\rho_w \left[\frac{\partial h_f C_w \tilde{T}}{\partial t} + \mathrm{div}(\bar{\mathbf{u}} h_f C_w \tilde{T})\right] \\ &\quad = \left[C_w \tilde{T}_{d,\infty} + \frac{\|\mathbf{u}_d\|^2}{2}\right] \times U_\infty \mathrm{LWC}\beta - 0.5(L_{\text{evap}} + L_{\text{subl}})\dot{m}_{\text{evap}} \\ &\quad + (L_{\text{fusion}} - C_{\text{ice}}\tilde{T})\dot{m}_{\text{ice}} + \varepsilon\sigma(T_\infty^4 - T^4) + \dot{Q}_h \end{aligned} \tag{5}$$

where the first three terms on the right-hand-side model correspond, respectively, to the heat transfer caused by the supercooled water droplets impingement, the evaporation, and the ice accretion. The last two terms represent the radiative and convective heat transfer. Based on the work of Hedde [11], half of the water is considered liquid and the other half considered solid when evaporation occurs. The heat loss by radiation is included, although it is important only in anti-icing simulation. Conduction through the metal skin is neglected, based on the fact that ice acts as an insulator [12].

The convective heat transfer calculated by the flow solver is converted into a heat transfer coefficient before ice accretion calculations. The heat transfer coefficient depends only weakly on the surface temperature distribution along the airfoil, but will change depending on the boundary-layer thickness. The coefficients ρ_w, C_w, C_{ice}, L_{evap}, L_{subl}, L_{fusion}, and σ represent physical properties, whereas $\tilde{T}_{d,\infty}$, U_∞, liquid water content (LWC), and T_∞ are airflow and droplet parameters specified by the user. The Eulerian droplet module provides local values for the collection efficiency β and the droplet impact velocity $\mathbf{u}_d$. The flow solver provides the local wall shear stress τ_{wall} and the convective heat flux $\dot{Q}_h$. The evaporative mass flux is recovered from the convective heat flux using a parametric model [13]. Compatibility relations are incorporated to close the system.

The discretization of the equations is via a finite volume method. The hull of the three-dimensional mesh at the air-structure/ice-shape interface is called the surface mesh. From the surface mesh, a dual surface mesh is obtained by connecting the baricenters of the surface mesh cells to the midedges of the cells. The unknowns are computed at the center of each cell, thus corresponding one to one to the nodes of the finite element grid used for the air and droplet solutions.

The transport-type equations solved in FENSAP-ICE (FENSAP, DROP3D, and ICE3D) are computationally demanding, requiring one to two days for a single flight condition. In the present work, FENSAP-ICE is used to obtain a limited number of high-fidelity snapshots and the POD method is studied as an appropriate ROM to rapidly reconstruct the flow, the liquid water distribution, and the ice shapes for other flight conditions within the set of snapshots computed via FENSAP-ICE.

B. Proper Orthogonal Decomposition as a Reduced-Order Model

We select the Karhunen–Loéve [14] components analysis, commonly known as the POD method, a popular approach to obtain ROMs for computationally intensive applications [15–17]. The core of the POD method is the extraction of a set of eigenfunctions that describes the dominant features of the flow. Once these eigenfunctions are calculated, a simple projection of the CFD model onto the space spanned by the POD eigenfunctions yields ROMs.

The method of snapshots, first introduced by Sirovich [18], provides a convenient means to compute these eigenfunctions. As an example of its application to complex aerodynamic flows, solutions with varying Mach numbers and angles of attack (AOA) could be precomputed, and these samples then used to compute the POD eigenfunctions of the ROMs, which are then used to rapidly predict the flow at any other Mach number and AOA within the span of values selected.

POD, also known as the principal component analysis, requires a data set (called snapshots) from the CFD solvers for the physical properties:

$$U^i = U(x^i, y^i, \ldots) \tag{6}$$

where x and y denote the variables that are of interest and are the subject of the parametric analysis. U is the vector with values for a certain combination of variables. This data set can be applied to any type of local or integrated flow variable, such as velocity, pressure, pressure coefficient, density, lift, drag, or ice thickness, as in this work. A set of snapshots are expressed by

$$U^{\text{snapshots}} = \{U^1, \ldots, U^M\} \tag{7}$$

Next, we compute the eigenfunctions from the data set, or snapshots. It starts with a set of snapshots and consideration about which function is most similar to the members of the snapshot set. To consider this, an averaging operation $\langle\,\rangle$ is needed for the variables. Mathematically, finding the optimal functions corresponds to finding ϕ as follows [19]:

$$\max\frac{\langle|(U,\phi)^2|\rangle}{(\phi,\phi)} = \frac{\langle|(U,\psi)^2|\rangle}{(\psi,\psi)} \tag{8}$$

In Eq. (8), (a, a) denotes the inner product:

$$(a, a) = \int_\Omega a(x)a^*(x)\,\mathrm{d}x \tag{9}$$

where a^* is the Hermitian conjugate of a, and $\mathbf{\Omega}$ denotes the spatial domain. This equation implies that one needs to find the value of ψ that yields the maximum values. This is a maximization problem (variational problem) in Eq. (8) of finding the value of ψ. While determining the value of ψ, there is a possibility of getting stuck in a local maximum of Eq. (8). To avoid this, we can constrain the denominator as $(\psi, \psi) = 1$. The problem then becomes a constrained maximization problem by

$$J[\psi] = \langle|(U,\psi)^2|\rangle - \lambda((\psi,\psi) - 1) \tag{10}$$

where λ is a Lagrange multiplier.

From the method of snapshots, developed by Sirovich [18], the eigenfunctions, ψ, to be solved are expressed as follows:

$$\psi = \sum_{i=1}^{M}\varpi^i U^i \tag{11}$$

where M is the number of snapshots. The eigenfunctions are composed of a linear combination of the snapshots. Substitution of Eq. (11) into the extremum of Eq. (10), the method of snapshots, yields

$$\frac{1}{M}\sum_{k=1}^{M}(U^i, U^k)\varpi^k = \lambda\varpi^i \tag{12}$$

The autocorrelation matrix from Eq. (12) is given by

$$R_{ij} = \frac{1}{M}\int_\Omega U^i(x,y)U^j(x,y)\,\mathrm{d}x\,\mathrm{d}y \tag{13}$$

where i and j are from 1 to M (M being the number of snapshots). We now have an eigenvalue problem written as

$$R\varpi = \lambda\varpi \qquad (\text{of size}\, M) \tag{14}$$

The matrix to solve becomes much smaller, reducing from a size N (the number of grid points) to a size M (number of snapshots). This is one of the advantages of using the POD technique. The resulting basis functions ϖ are fully orthogonal as they are eigenvectors from Eq. (14).

Once the eigenvectors are obtained, the POD eigenfunctions can be calculated using Eq. (11). The eigenvalues obtained from Eq. (11) determine the energy contained in each eigenfunction. The ratio of the energy contained in a certain mode (ith mode) can be measured by

$$\text{Energy} = \frac{\lambda_i}{\sum_{j=1}^{M}\lambda_j} \tag{15}$$

The approximation by POD calculation of the linear combination of eigenfunctions can be written as

$$U^{\text{POD}} = \sum_{i=1}^{l}\alpha^i\psi^i \tag{16}$$

where l is the number of modes used for the construction of the approximation by POD, so that $M \geq l$. α^i is a set of coefficients for the eigenfunctions. These are calculated by

$$\alpha_i^t = (\psi^i, U^t) \tag{17}$$

where ψ^i denotes the eigenfunctions corresponding to the ith mode of the POD eigenfunction, and U^t denotes the snapshots corresponding to the tth field. Note that $\{\alpha_i^t\}_{i=1}^M$ is a function of variables used for the parametric analysis. To predict a field that is not part of the snapshots, an interpolation method must be employed to obtain the coefficients $\{\alpha_i^{\delta t}\}_{i=1}^M$. Once $\{\alpha_i^{\delta t}\}_{i=1}^M$ is calculated for the uncalculated variable case of ∂t, the prediction can be done using Eq. (16). Interpolation methods such as linear, cubic spline, and Akima can be employed to compute the coefficients. As cubic splines are well understood, only the Akima technique is discussed herein.

C. Akima Approach as an Interpolation Method

Cubic splines often generate unnatural wiggles, and this is overcome by the Akima interpolation, which uses third-order polynomials but is more like a hand-drawing interpolation scheme.

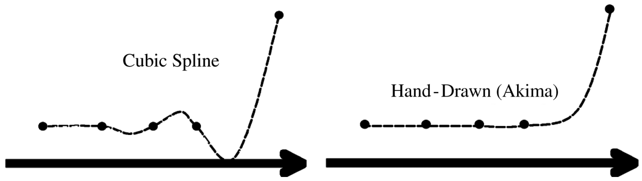

Fig. 1 Contrast between cubic-spline and Akima interpolations.

Figure 1 illustrates the difference between the cubic-spline and the Akima approaches. The dots represent the data points or snapshots. In the case of the cubic-spline approach, large oscillations appear between the points and, thus, produce incorrect results. To prevent these oscillations, a larger number of snapshots are required. However, in the case of the Akima interpolation, a horizontal line is produced between the first and fourth points, and a third-order polynomial between the last two points. This closely reflects a hand-drawn interpolation through the five points [20]. The Akima approach employs only neighboring information to compute the local properties of the polynomial, unlike the cubic-spline approach, which uses global information.

With known values $f_i = f(x_i)$ for $i = 1, \ldots, N$, the interpolating function in one dimension is defined as

$$\begin{aligned} f(x) &= a_1 + a_2(x - x_i) + a_3(x - x_i)^2 \\ &\quad + a_4(x - x_i)^3, \qquad x_i \leq x \leq x_{i+1} \end{aligned} \tag{18}$$

Next, to determine the values of $a_1 \sim a_4$, the values of f_i, f_{i+1}, f'_i, and f'_{i+1} are used. Those coefficients are defined as

$$\begin{gathered} a_1 = f_i \qquad a_2 = f'_i \qquad a_3 = \frac{3d_i - 2y'_i - y'_{i+1}}{x_{i+1} - x_i} \\ a_4 = \frac{y'_i + y'_{i+1} - 2d_i}{(x_{i+1} - x_i)} \qquad d_j = \frac{f_{j+1} - f_j}{x_{j+1} - x_j}, \qquad j = i - 2, \ldots, i + 1 \end{gathered} \tag{19}$$

Using d_i, weighting coefficients are defined as

$$W_{i-1} = |d_{i+1} - di| \qquad W_i = |d_{i-1} - d_{i-2}| \tag{20}$$

Derivatives of the function are given by

$$\begin{array}{llll} f'_i = \dfrac{W_{i-1}d_{i-1} + W_i d_i}{W_{i-1} + W_i} & & f'_i = d_{i-1} & d_{i-2} = d_{i-1} \\ d_i \neq d_{i+1} & f'_i = d_i & d_i = d_{i+1}, & d_{i-2} \neq d_{i-1} \\ f'_i = \dfrac{d_{i-1} + d_i}{2} & & \multicolumn{2}{l}{d_{i-2} = d_{i-1} \neq d_i = d_{i+1}} \end{array} \tag{21}$$

and boundary conditions at s_1, s_2, s_{N-1}, and s_N are considered:

$$\begin{aligned} d_{-1} &= 2d_0 - d_1 \\ d_0 &= 2d_1 - d_2 \\ d_N &= 2d_{N-1} - d_{N-2} \\ d_{N+1} &= 2d_N - d_{N-1} \end{aligned}$$

This procedure can be extended to multidimensional surfaces and to unstructured grids [21].

III. Methodology of Reconstructing Airflow and Icing Parameters

The aim of this work is to demonstrate the effectiveness of applying POD to aerodynamic and aero-icing flows. The procedure to reconstruct the flow or icing from the snapshots in a two-variable problem is as follows. First, select a limited number of snapshots by varying each variable. The variables are generally selected from a list of flight-condition parameters, such as the freestream Mach number, temperature, and angle of attack, or integrated flow quantities, such as the lift or drag coefficients. Once the variables are selected, the natural next step is to identify the range of values for each variable. At a cruise flight condition, a Mach number range between 0.2 and 0.4 would be an appropriate range of speeds during icing encounters. In the case of the freestream temperature, the temperature range should include both glaze and rime ice conditions. Once the range is specified, a select number of cases must be chosen by varying the variable. As stated in the previous section, a larger number of snapshots would certainly produce a more accurate POD model; however, it would also dramatically increase the computational cost. For the results demonstrated in this work, five to seven snapshots were employed for each variable, with additional snapshots at regions of higher nonlinearity based on a priori knowledge of the flow conditions.

Second, apply the POD method to compute the eigenfunctions as specified in Eqs. (11) and (14). The process begins with the computation of the autocorrelation matrix as shown in Eq. (13) by performing a dot product of the vector of snapshots. The next step is to solve Eq. (14) for the eigenvalues and eigenvectors using existing libraries. In this work, the LAPACK version 3.1 was employed. Once the eigenvectors are obtained, the eigenfunctions are evaluated using Eq. (11), in which the eigenfunctions are composed of a linear combination of the snapshots.

Third, interpolate the coefficients of the basis function using either a linear, cubic-spline, or the Akima interpolation technique as mentioned in detail in Sec. II.B.

Lastly, the POD solutions can be obtained as a linear combination of the eigenfunctions as stated in Eq. (16). The following results use the aforementioned four-step process to compute the POD solutions. Details of the type of variables employed and the choice of the snapshots are provided for each test case.

IV. Results: Two-Dimensional NACA 0012 Case

The POD method is applied to the reconstruction of ice shapes for 2-D viscous flow under a one-variable problem, here being freestream temperature. First, ice-shape predictions for various freestream temperatures are presented. The effect of the number of POD modes, number of snapshots, and the choice of snapshots on the predicted ice shapes is then investigated.

A. Ice-Shape Prediction: Effect of Temperature Variation

We first investigate the effectiveness of the POD approach in reconstructing ice shapes around a NACA 0012 airfoil and study the impact of the freestream temperature on the POD-reconstructed ice shapes. Figure 2 illustrates a structured viscous mesh with 1.4×10^6 nodes. A concentration of cells is placed around the surface to effectively capture the boundary layer. The numerical simulations are computed for a Mach number of 0.32 and Reynolds number of

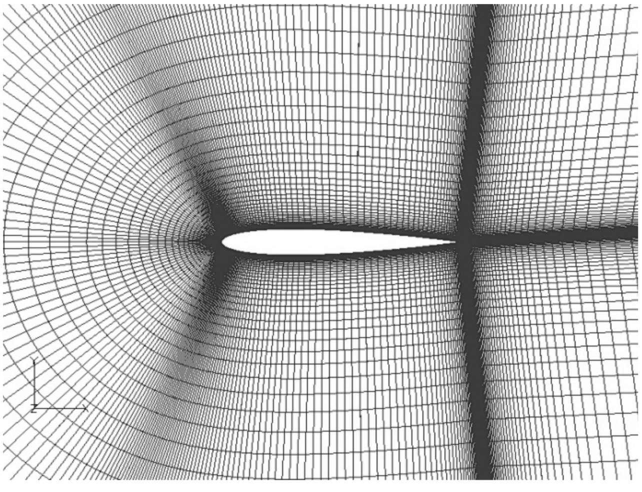

Fig. 2 Structured mesh for the NACA 0012 airfoil.

4.6×10^6. The freestream total temperature ranges from 12 to 28°F, such that both glaze and rime ice shapes are generated. A total of eight FENSAP-ICE computations are performed at freestream total temperatures of 12, 15, 18, 19, 21, 22, 25, and 28°. The flight-condition parameters for both DROP3D and ICE3D are as follows: the LWC and MVD are set to 0.55 $\mathrm{g/m^3}$ and 20 μm and the total ice accretion time is 420 s. Figure 3 illustrates the convergence history of the total residual for the FENSAP code. The residual drops 7 orders of magnitude within 4000 iterations. For most of the typical runs, the simulations were halted after a 4 order of magnitude drop because this is sufficient for both the lift and drag coefficients to be considered converged. In Fig. 4, the convergence of α is demonstrated for the DROP3D code. Figure 5 shows the convergence of the total ice mass for the ICE3D code.

Figure 6 illustrates the ice accretion for all eight temperature cases. It shows that, at the higher temperature, a stronger nonlinearity is observed. Between the 25 and 28° cases, a 3° difference results in dissimilar ice shapes, with the characteristic horn shapes appearing. The upper horn at the higher temperature seems to be larger, as well as the lower horn. As the temperature is reduced, water freezes directly on impact, reducing the amount of runback; thus, the horn shapes are less pronounced. At the lower temperatures, the changes are minimal except for a slight reduction in the size of the two spikes observed at the mid-leading-edge region. The apparent greater variation of the ice shapes at higher temperature indicates that a larger number of snapshots should be used in this temperature range to enrich the database of the POD algorithm.

The next step is to generate ice shapes using the POD approach based on the snapshots and compare them using the full FENSAP-ICE sequence. For the first test case, we compare a FENSAP-ICE solution at 20°F to that of a reconstructed ice shape by POD. The coefficients for the POD analysis are computed using the cubic-spline approach. Figure 7 compares the POD solution to that acquired through FENSAP-ICE. The POD analysis reproduces the total thickness of the accreted ice remarkably well. However, there is a slight disagreement at the two horns, which are characteristics of glaze ice. The horns have a large effect on the flowfield downstream of the leading edge and greatly influence the overall aerodynamic performance of the airfoil. A conservative prediction of the horns could ultimately underestimate the performance degradation. Thus, it is of vital importance that in this exercise we investigate the following: first, the number of modes required to reconstruct the

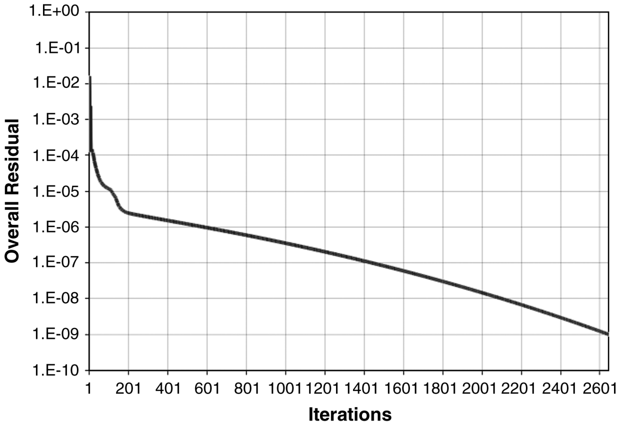

Fig. 3 Convergence history of FENSAP (flow), overall residual.

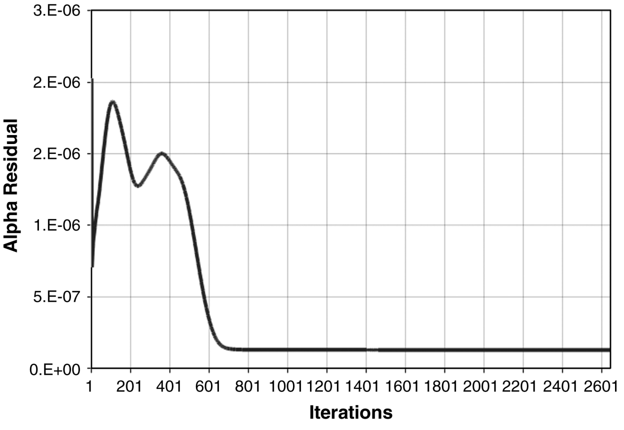

Fig. 4 Convergence history of DROP3D, alpha residual.

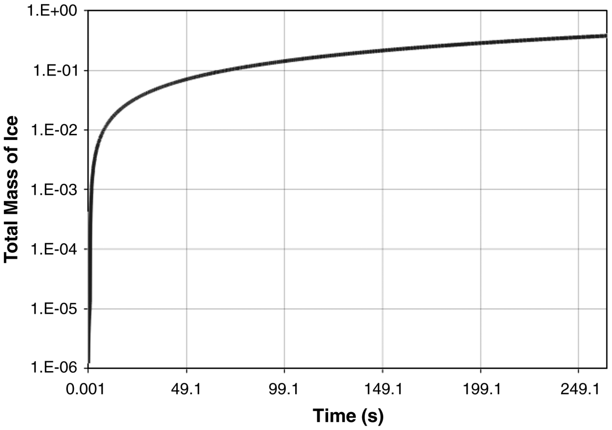

Fig. 5 Convergence history of ICE3D, total mass of ice.

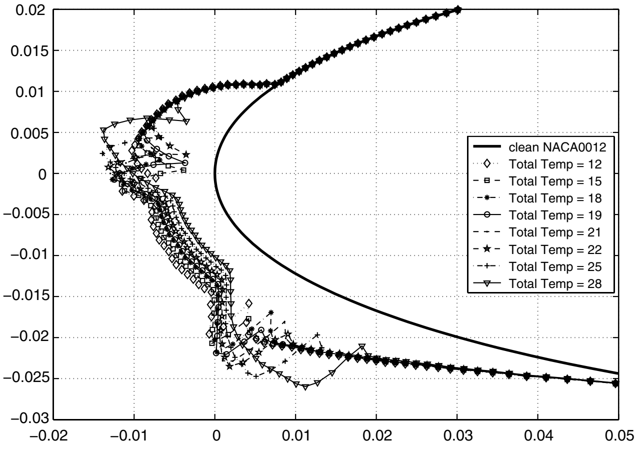

Fig. 6 Ice-shape change around the leading edge for different total temperatures computed by FENSAP-ICE.

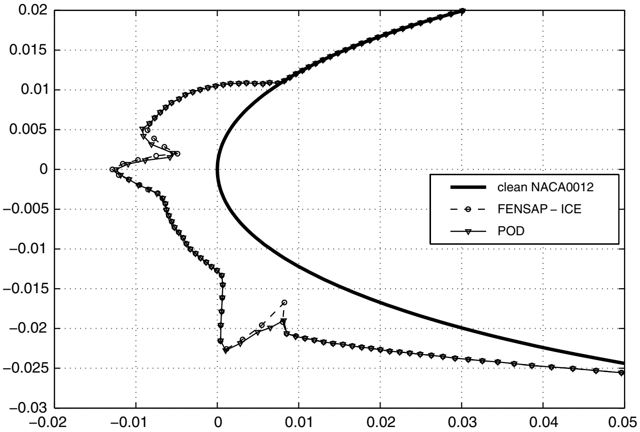

Fig. 7 Ice-shape comparison at a temperature of 20°F using eight snapshots at temperature = 12, 15, 18, 19, 21, 22, 25, and 28°F.

solution; second, the minimum number of snapshots needed to reconstruct accurate ice shapes at any total temperature; and third, the placement of the snapshots within the range of the total temperature.

B. Ice-Shape Prediction: Effect and Role of Number of Proper Orthogonal Decomposition Modes

We investigate the effect of number of modes on the reconstructed POD solution at a freestream total temperature of 20°, using six snapshots at 12, 15, 18, 22, 25, and 28°F. The number of snapshots has also been dropped from eight to six by removing the solutions at 19 and 21°F, as the POD coefficients in this temperature range are linear for the first three modes. A detailed analysis will be shown in the next paragraph. Figure 8 illustrates the change in ice shapes with an increasing number of modes. One mode, represented by the line with diamonds, signifies that only the first POD mode is employed to compute the final ice shape; consequently, the line with the asterisks denotes that the first two modes are included. The high-fidelity FENSAP-ICE solution is represented by the dashed line. The figure demonstrates that the first and second modes represent the ice accretion thickness, as it exactly matches the FENSAP-ICE solution at the midpoint. However, neither mode captures the horns, although their presence is visible. The inclusion of the third mode, indicated by the line with squares, brings into the picture the upper horn but not the lower horn. The fourth mode, portrayed by the line with circles, finally brings in the lower horn. The addition of the fifth and higher modes further refines the solutions, but does not add any new key feature to the ice shape. In summary, the nonlinear phenomena governing ice accretion can be captured by four fundamental modes, the first and second being vital to obtain the ice thickness and the third and fourth modes providing the shape of the upper and lower horns, respectively, and distinctively.

Figures 9–11 illustrate the coefficient distributions interpolated by cubic splines for the first, second, and third modes in the x coordinate direction. The coefficient for the first mode is almost constant over the range of temperatures, with a variation of the order of 10^{-4}. The values are virtually constant and linear at the lower temperatures but small oscillations are observed after a freestream temperature of 13°. In Figs. 10 and 11, the coefficients exhibit a linear response between 0 and 13°. Figure 10 illustrates a line with a positive slope, and Fig. 11 illustrates an almost horizontal line. However, above 13°, the coefficients display a higher degree of nonlinearity. In this temperature range, due to the presence of water runback and the particular flow physics associated with it, ice accretion displays a higher degree of nonlinearity known as glaze ice. As seen earlier, additional snapshots were required at the higher temperatures due to the larger changes in the ice shapes. The degree of nonlinearity increases with temperature. Figures 12–14 show the coefficient distributions for the first, second, and third modes along the y coordinate. All three curves exhibit linear distributions until 11 or 13°F. As illustrated earlier, this behavior is related to the physics of the flow and the manner in which rime and glaze ice are formed. In the latter case, a higher degree of nonlinearity is observed.

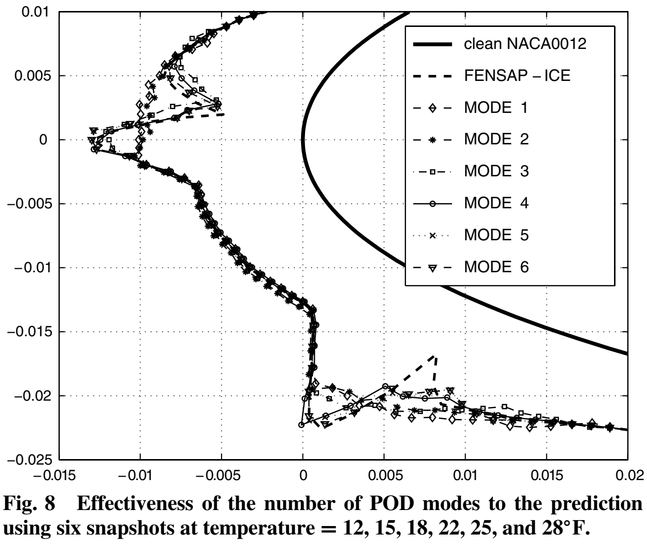

Fig. 8 Effectiveness of the number of POD modes to the prediction using six snapshots at temperature = 12, 15, 18, 22, 25, and 28°F.

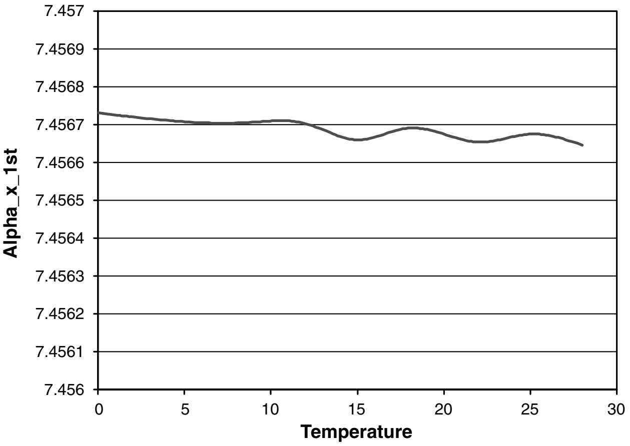

Fig. 9 Coefficient of first mode for x coordinate.

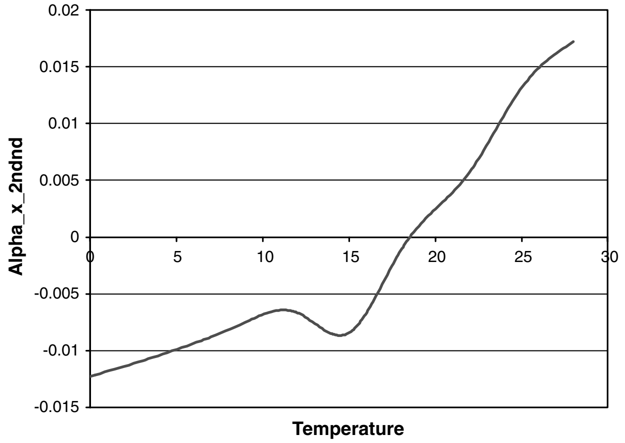

Fig. 10 Coefficient of second mode for x coordinate.

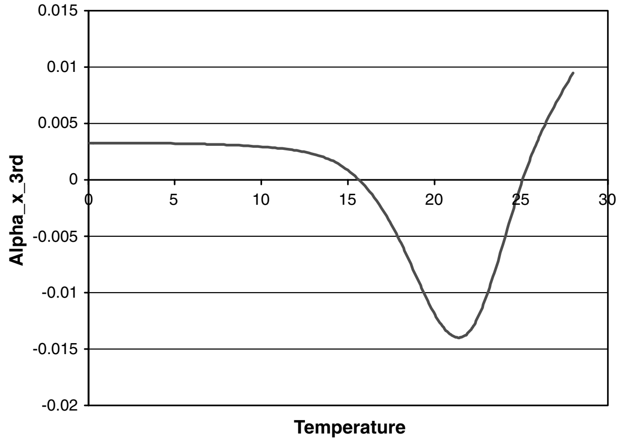

Fig. 11 Coefficient of third mode for x coordinate.

In summary, the analysis of the mode shapes in both the x and y directions provide a deeper understanding of the physics of the flowfield. The nonlinearity in the mode shapes after a certain temperature indicates that the additional snapshots should be placed in these regions to increase the accuracy of the POD-based reconstructed solution.

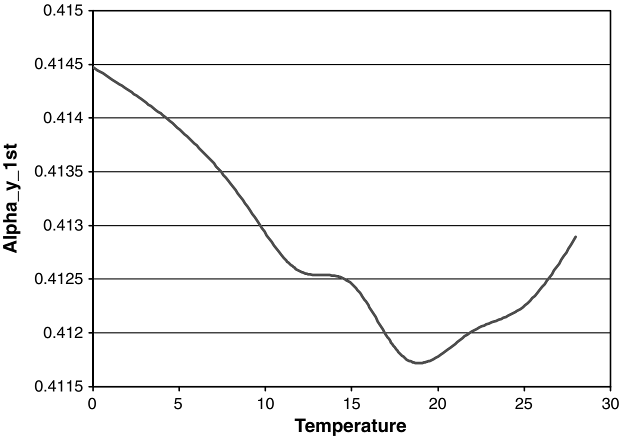

Fig. 12 Coefficient of first mode for *y* coordinate.

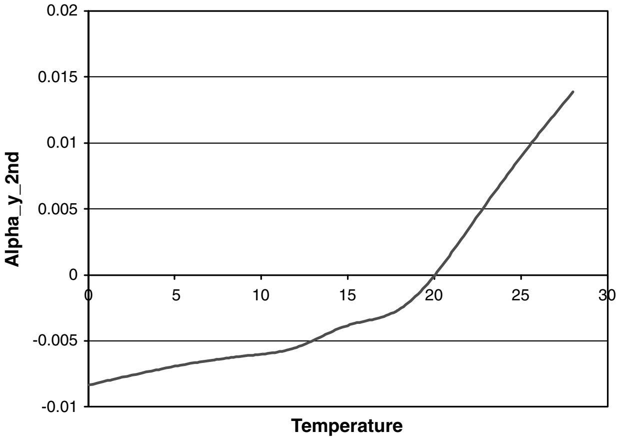

Fig. 13 Coefficient of second mode for *y* coordinate.

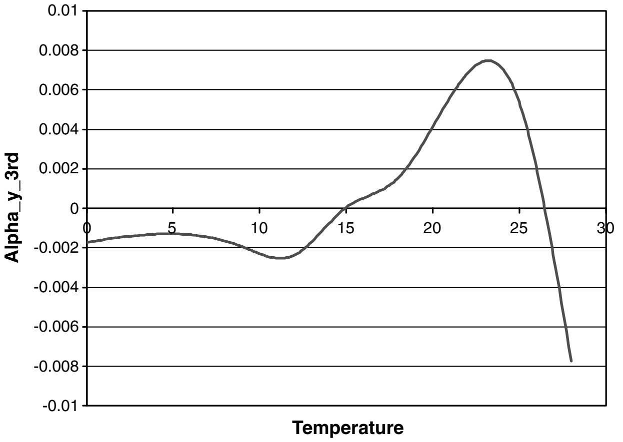

Fig. 14 Coefficient of third mode for *y* coordinate.

C. Ice-Shape Prediction: Minimum Number and Selection of Snapshots

We investigate the consequence of reducing the number of snapshots. In Fig. 15, the accreted ice shape is compared between the FENSAP-ICE and POD solutions at the same freestream total temperature of 20°F, without the 19 and 21°F cases of the case in Fig. 7, thus reducing the total number of snapshots from eight to six. As mentioned in Sec. IV.B, these snapshots were selected for removal because the distribution of coefficients for the first three modes are linear in this range; thus, the omission of these snapshots should not affect the solution. The POD solution, as shown in Fig. 15, compares well with a high-fidelity capture of the ice thickness, and location, size, and shape of the horns. A slightly larger discrepancy is observed at the lower horn, where the predicted indentation at the base of the horn is less pronounced when compared to the FENSAP-ICE solution and the POD solution with eight snapshots.

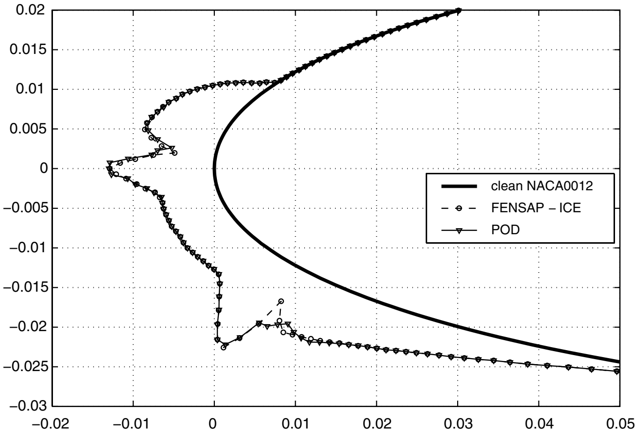

Fig. 15 Ice-shape comparison at a freestream total temperature of 20°F using six snapshots at $T = 12, 15, 18, 22, 25,$ and 28°F.

In the second test case, the number of snapshots is reduced to five by further eliminating the snapshot at 18°F. The coefficients are largely linear in this range, except for the coefficient of the first mode for the *y* coordinate, where the solution at the 18°F freestream temperature defines the reversal of the slope of the line. Therefore, the removal of this snapshot is expected to have a larger effect on the POD solution. Figure 16 illustrates that the general shape of the accreted ice is reconstructed accurately; however, there are greater discrepancies at the horns. First, the maximum thickness of the upper horn is slightly underpredicted, and second, the location of the lower horn is incorrect. Lastly, to illustrate further the removal of important snapshots, a four-snapshot POD solution is generated using solutions from the 12, 15, 25, and 28°F, with further elimination of the snapshot at the 22°F freestream temperature. Figures 11–14 illustrate that the solution at this temperature is critical in defining the reversal of the slope of the lines for the third mode for both the *x* and *y* coordinates. Figure 17 illustrates that the two solutions agree well on thickness of the accreted ice; however, the location, size, and shape of the horns are vastly dissimilar. This illustrates that the snapshot at 22° was crucial in preserving the horn shapes and locations. Thus the five-snapshot case, with snapshots from 12, 15, 22, 25, and 28°, was sufficient to acquire ice shapes that incorporate the principal features, such as ice thickness and horn shapes and locations. However, the six-snapshot case provided better results.

In summary, reducing the number of snapshots has the effect of decreasing the quality of the POD-reconstructed solution, as

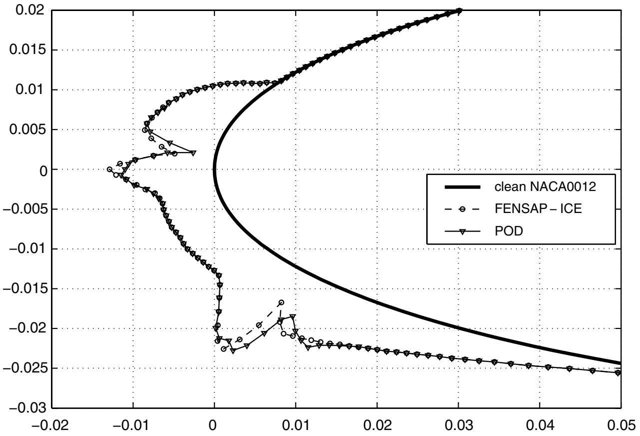

Fig. 16 Ice-shape comparison at a freestream total temperature of 20°F using five snapshots at $T = 12, 15, 22, 25,$ and 28°F.

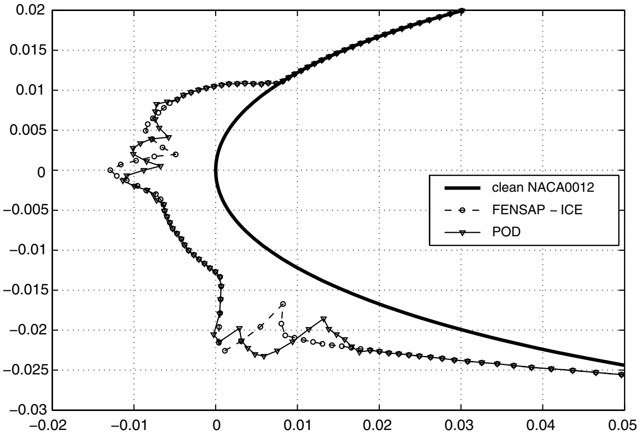

Fig. 17 Ice-shape comparison using four snapshots at temperature= 12, 15, 25, and 28°F.

expected. The ice accretion and the size and shape of the horn were highly dependent on the freestream temperatures in the limits of the temperature range. At the higher temperature range, the size and shape of the horns were greatly affected, whereas at the lower limit, it was the thickness of ice. To represent these changes, it is important to preserve snapshots at either limits and, if needed, eliminate ones that are in the midrange.

Next, we compare the FENSAP-ICE high-fidelity solution to that computed by the POD approach at a given freestream temperature. As concluded from the preceding paragraphs, six snapshots at 12, 15, 18, 22, 25, and 28° provide the best possible solution with the least number of cases. This set of snapshots will be used for this test case. A freestream temperature of 26.5° is chosen because large changes in the size and shape of the horns are observed at these temperatures, as illustrated in Fig. 6. This temperature is slightly below the freezing temperature and it has a strong water runback, causing glaze ice. Figure 18 compares the POD and FENSAP-ICE solutions. The general shape of the ice is reconstructed well, with an excellent capture of the ice thickness and the location and general shape of the horns. A small difference is observed at the two horns. At the upper horn, an indentation exists to form two subhorns, whereas the FENSAP-ICE solution only shows a single horn. At the lower surface, a small difference between the locations of the groove is observed.

V. Results: Three-Dimensional DLR-F6 Case

In this section, we demonstrate the effectiveness of the POD approach at reconstructing the flow and ice shapes over a complete aircraft. The chosen geometry is the DLR-F6, created as part of the AIAA CFD Drag Prediction Workshop [22]. The simulations are performed for the approach flight condition, an important flight regime for ice accretion as the aircraft approaches at close to stall speed and the aerodynamics degradation due to ice formation is an important aspect. The LWC and MVD are set to 0.001 kg/m^3 and 20 μm, the ice accretion time is set to 180 s, and the Mach number and other freestream conditions are frozen for all the runs. However, the AOA and freestream temperature are varied to generate results for the various cases or snapshots.

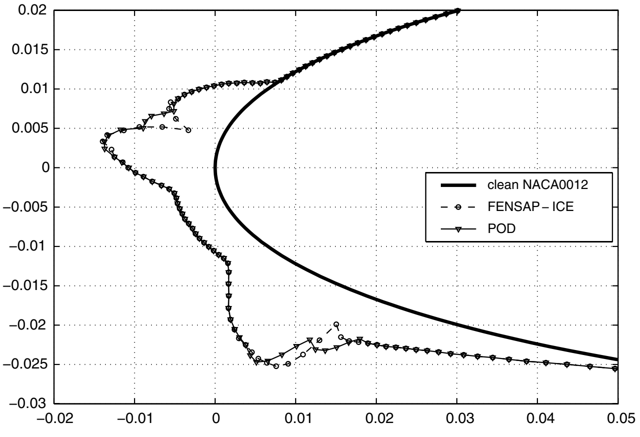

Fig. 18 Ice-shape comparison for highly nonlinear region at temperature = 26.5°F.

A. Computation Cycle for Temperature and Angle of Attack Variation

To gather the snapshots for the POD application, a range of freestream temperatures and AOA are considered. As mentioned earlier, three successive computations, FENSAP (flow), DROP3D (water concentration), and ICE3D (ice accretion), have to be conducted to compute the ice shape. To reduce the total computational time, solutions for the water concentration have only been computed for each AOA, while freezing the LWC at each AOA. Hence, in this work, LWC is approximated to be constant for all the temperatures shown. The computation cycle conducted in this work is shown in Fig. 19.

B. Gathering Snapshots; FENSAP-ICE Solutions

In this section, the FENSAP-ICE numerical solutions are presented. The flight conditions for all the test cases are based on the following analysis. The DLR-F6 configuration is designed based on a wide-body Airbus aircraft such as the A300-600R.[§] Therefore, the flight-condition parameters at an approach phase are computed based on this particular aircraft; thus, the approach Mach number is 0.235 and the reference temperature is 260 K. To generate the various snapshots, both the AOA and freestream temperature are varied as follows:

$$\text{AOA} = 0, 4, 8, 12, \text{ and } 16 \text{ (deg)}$$

$$\text{temperature} = 265, 263, 260, 257, \text{ and } 254 \text{ (K)}$$

These two parameters were chosen because they have a large influence on the ice formation and, ultimately, the performance degradation of the aircraft. The freestream Mach number plays an important role as well; however, we chose to restrict the snapshots as a function of only two variables. Therefore, in total, 25 (5×5) snapshots are computed.

Figure 20 illustrates the DLR-F6 grid, for which the geometry contains only the fuselage and wing. The mesh has 1.22×10^6 nodes and 3.9×10^6 elements, and the far-field boundary is placed approximately 15 body lengths from the aircraft surface. ICEM-CFD was employed to generate the grid around the DLR-F6. In Fig. 21, a cross-sectional cut along the aircraft wing is shown, with prism layers at the surface to capture the boundary-layer effects. Figure 22 illustrates the pressure distribution on the surface of the DLR-F6 at an AOA of 4 deg, freestream Mach number of 0.235, and freestream total temperature of 265 K. The total run time for all three codes was approximately four days on a 16 CPU AMD Opteron cluster equipped with an InfiniBand Switch for data communication. Figure 23 illustrates the LWC distribution. The intensity of the LWC is concentrated on the leading edge of the wing and the fuselage nose. Figure 24 shows the ice thickness accreted at a freestream temperature of 265 K. The figure demonstrates that ice is formed around the fuselage nose within the first 10% of the fuselage length, as well as the entire length of the leading edge of the aircraft wing, with the majority close to the wing root.

To further accentuate the accreted ice shapes at various span stations, Fig. 25 illustrates the ice shape at four different span locations for the same test case. As shown, a large horn, characteristic of glaze ice, is formed. In Fig. 26, ice shapes are illustrated at the

---

[§] Data available online at http://www.airbus.com/en/aircraftfamilies/a300a310/a300-600/specifications [retrieved 2 December 2009].

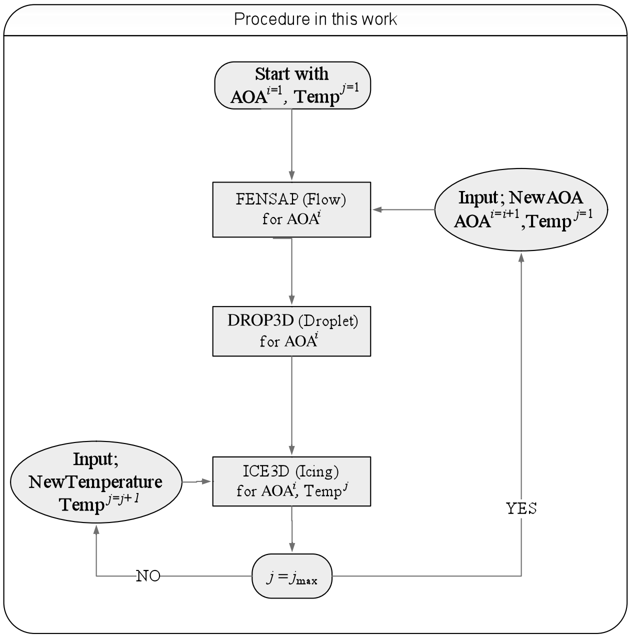

Fig. 19 Procedure of icing computation.

midspan for various angles of attack at a freestream temperature of 265 K. The dark gray line corresponds to the 0 deg case, whereas the light gray line coincides with the 16 deg solution. At the lower angles of attack, the majority of ice forms around the leading edge and centers about the stagnation point. A large horn shape is observed on both the lower and upper surfaces, and ice formation is absent in the trailing-edge region. At higher angles of attack, the majority of ice is formed on the lower surface. The large horn is replaced by a rather smooth curve that extends from the leading edge to 50% of the chord on the lower surface. Ice is also present at the trailing edge. This figure demonstrates that, as expected, AOA plays a very important role in the formation of ice on aircraft wings and the behavior is highly nonlinear.

Figure 27 shows the ice shapes at the midspan for various temperatures at angles of attack of 4 and 16 deg. The light gray line corresponds to the ice shape at 265 K and the dark gray line at 254 K. Both figures reaffirm the fact that, although at lower temperatures the ice accretion is larger, the general shape of the ice is fairly consistent throughout the range of temperatures. A comparison of Figs. 26 and 27 suggests that the AOA plays the greatest role in the determination of the final ice shape.

C. Ice-Shape Comparison Between FENSAP-ICE and Proper Orthogonal Decomposition

In this section, we compare the three-dimensional ice shapes and calculation times between FENSAP-ICE and two POD solutions obtained with the cubic-spline and Akima interpolation schemes. The solutions were obtained at an AOA of 6 deg and freestream temperature of 261.5 K. Figures 28–30 illustrate the three solutions around the DLR-F6. Both the POD solutions visually compare very well to the solution provided by FENSAP-ICE. It is impressive to note that the POD solutions are obtained in 6–10 min, compared to four days for the FENSAP-ICE calculations, that is, a speedup of over 600–1000 times.

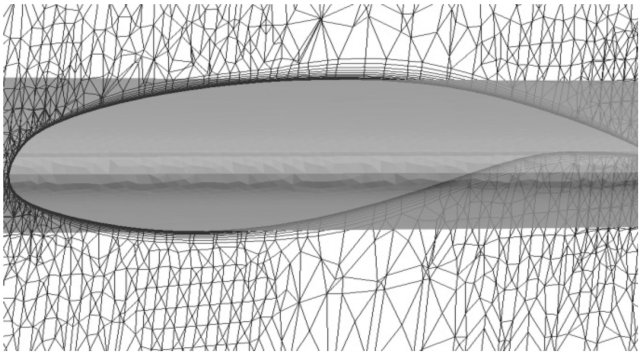

Fig. 21 Prismatic layers around body.

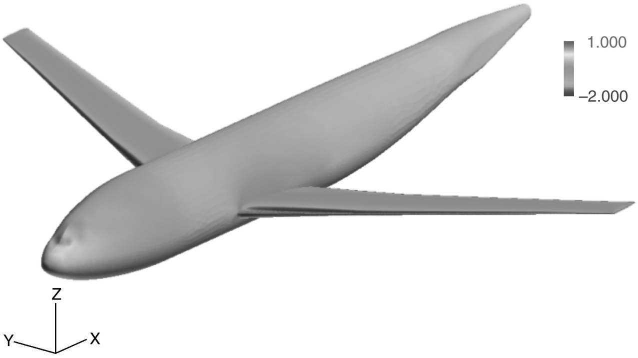

Fig. 22 Pressure coefficient on surface of DLR-F6.

Ice is observed at both the leading edge of the aircraft wing and the fuselage nose. A slight disagreement is observed at the lower surface of the fuselage nose, where both POD solutions suggest the presence of ice. The large bulge close to the wing root is present in both POD solutions. A closer examination of the lower surface of the aircraft wing is made in Figs. 31–33. The overall comparison between the solutions is very good, with a slight difference on the lower surface, where the extent of ice accretion in the chordwise direction seems larger than in the FENSAP-ICE solution. However, a closer inspection of this region shows that the thickness of ice is negligible.

Figure 34 compares the POD solutions with FENSAP-ICE at an AOA of 6 deg and freestream temperature of 261.5 K at 10, 30, 50, 70, and 98% span locations. The shape of the ice both at the leading and trailing edges at all span locations are captured accurately; both POD solutions compare very well to the FENSAP-ICE solution. A

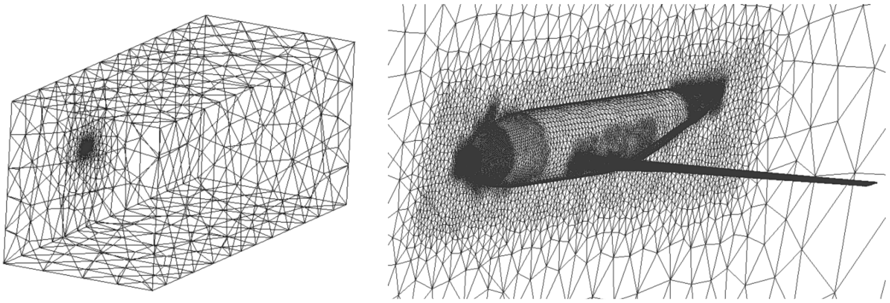

Fig. 20 Unstructured grid around DLR-F6.

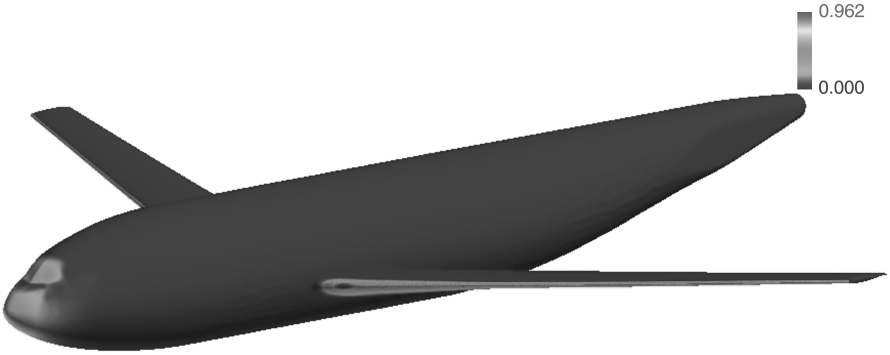

Fig. 23 LWC distribution on DLR-F6 from DROP3D.

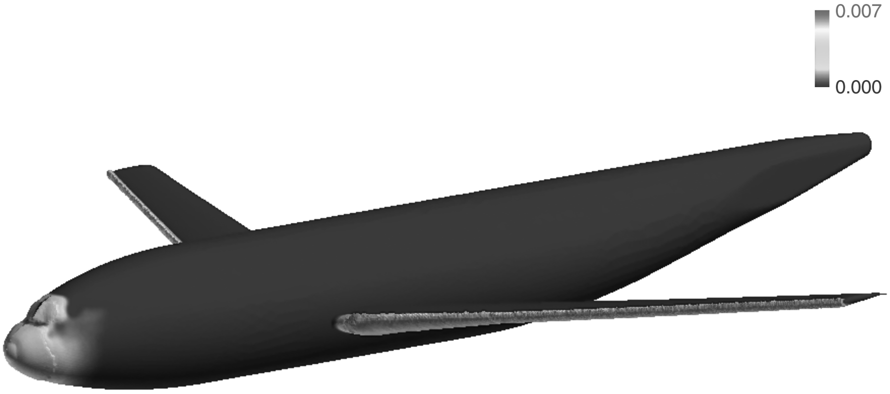

Fig. 24 Ice thickness distribution on DLR-F6 from ICE3D.

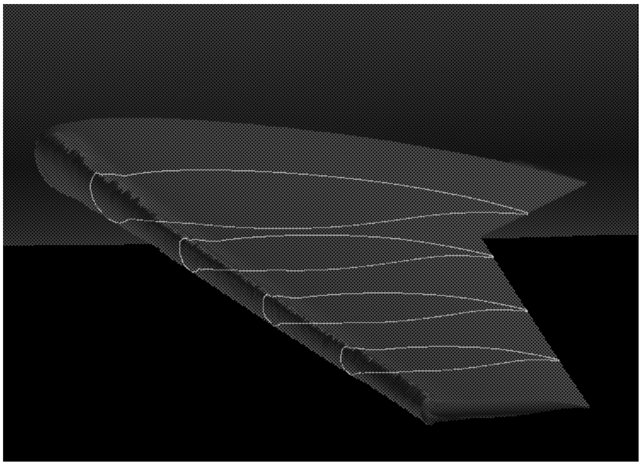

Fig. 25 Cross-sectional cuts of ice shapes.

close-up view of the leading edge at the 50 and 98% span locations is illustrated in Figs. 35a and 36a, in which the black line represents the FENSAP-ICE solution and the gray lines represent the POD solutions with cubic-spline and Akima interpolations. The general shape of the ice is captured very well by the POD solutions. There are slight differences at various chordwise locations, but the difference is marginal in comparison to the total thickness. The POD solutions match exactly, except for a small difference on the lower surface. At the trailing edge, as shown in Figs. 35b and 36b, a small difference is observed in the ice, but the general shape of the ice is reconstructed very well.

Figure 37 gives a map of the ice accretion, from rime to glaze ice, for various angles of attack and freestream temperatures. The solutions were computed in a matter of minutes. Such a capability provides aircraft manufacturers with a means to examine specific cases, as well as data that can be used to perform an analysis or design of the anti-icing system. The ice shapes can also be used to compute the lift and drag coefficients and provide the designer with a map of the performance degradation due to ice accretion for the entire flight envelope. In the case of application to flight simulators, operators could easily specify the flight-condition parameters and ice shapes, with the aerodynamics performance quickly computed for pilot training.

VI. Conclusions

In this paper, a POD approach to reduced-order modeling has been applied to the reconstruction of ice shapes for two- and three-

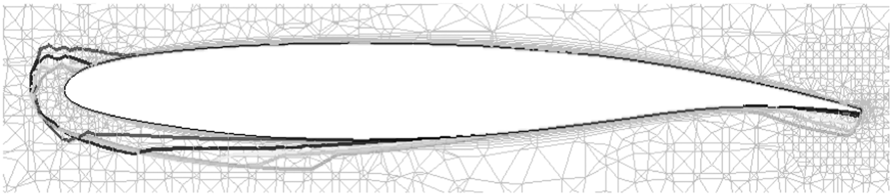

Fig. 26 Ice-shape change at midspan for different angles of attack from 0 to 16 deg at $T = 265$ K from FENSAP-ICE.

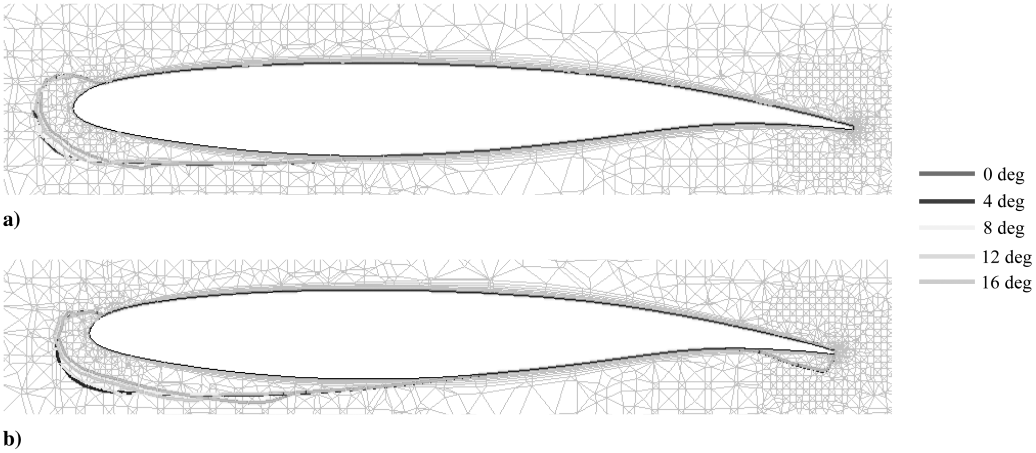

Fig. 27 Ice shapes at midspan for a range of freestream temperatures: a) AOA of 4 deg, b) AOA of 16 deg.

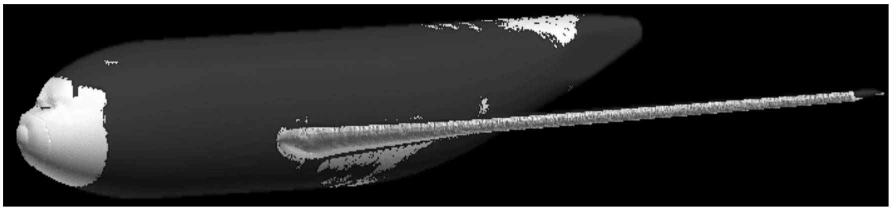

Fig. 28 Ice accretion on the DLR-F6 by FENSAP-ICE: FENSAP + DROP3D + ICE3D full calculations.

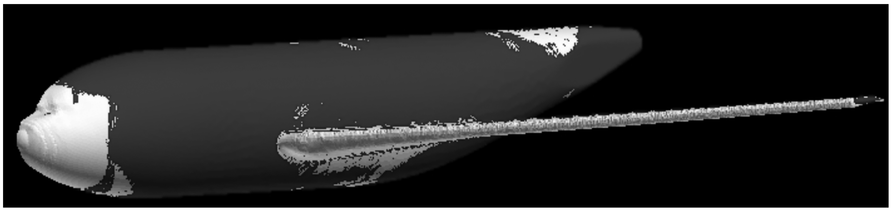

Fig. 29 Ice accretion on the DLR-F6 by POD using cubic spline.

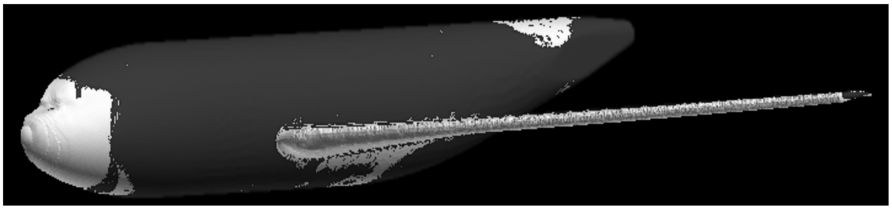

Fig. 30 Ice accretion on the DLR-F6 by POD using Akima interpolation.

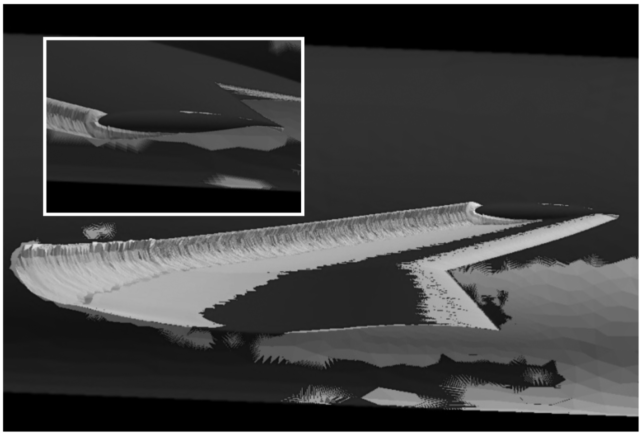

Fig. 31 Ice accretion around the wing by FENSAP-ICE.

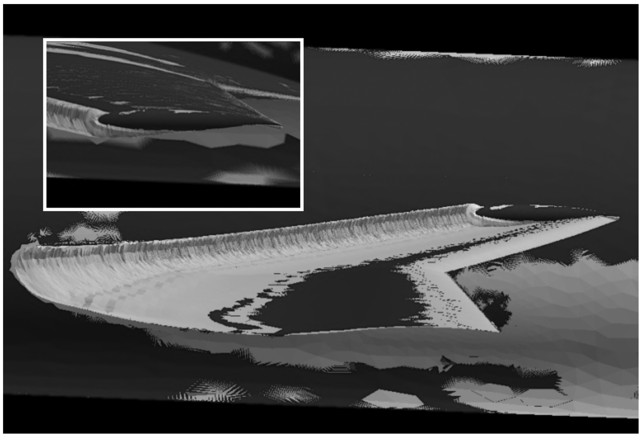

Fig. 32 Ice accretion around the wing by POD using cubic spline.

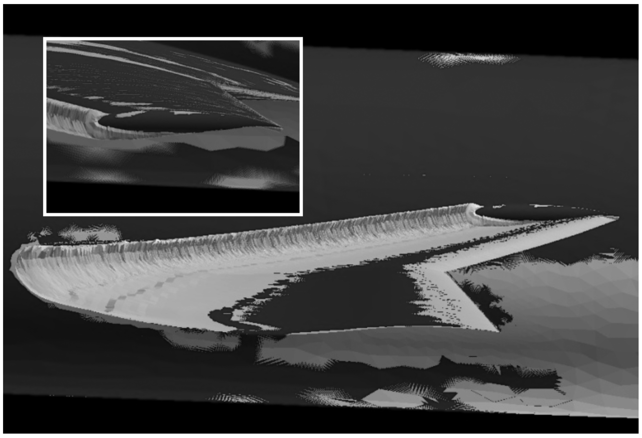

Fig. 33 Ice accretion around the wing by POD using Akima interpolation.

dimensional geometries. Both cubic-spline and Akima interpolation schemes proved efficient. The approach first demonstrates the effectiveness of the technique at reconstructing two- and three-dimensional ice shapes within a few seconds with modest computational resources, and then clearly identifies the effect of individual modes as well as the distribution of the coefficients on the sensitivity of the ice shapes to temperature and other flight conditions. It becomes evident that, as temperatures get higher than freezing, that is, for glaze ice, the proper choice of snapshots is vital to accurately reconstruct the ice shape.

Future applications may include extension to more than two variables for icing to include the effect of liquid water content, droplet size, pressure altitude, etc., to more completely explore the certification envelope and to extend the approach to the optimal design of anti- and de-icing systems and apply it to flight simulators.

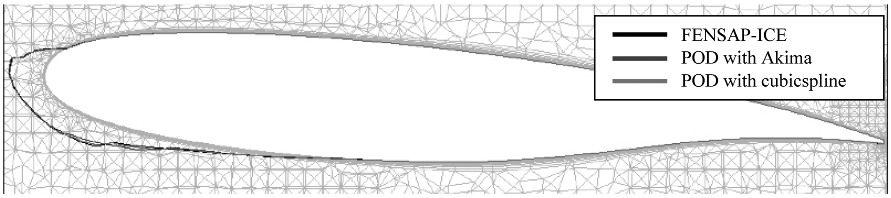

a) 10% span

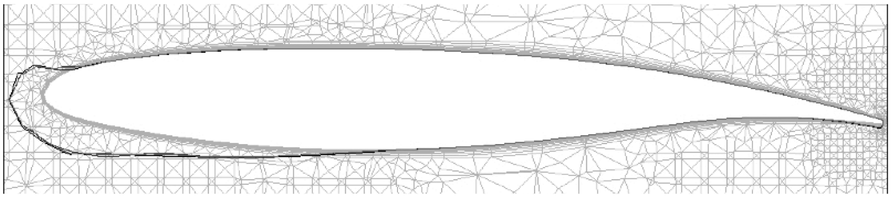

b) 30% span

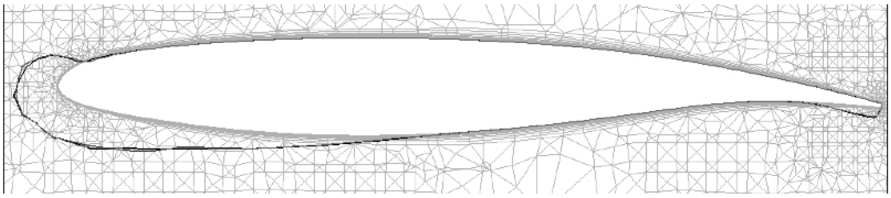

c) 50% span

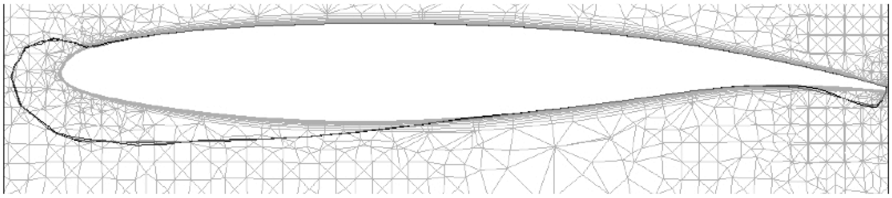

d) 70% span

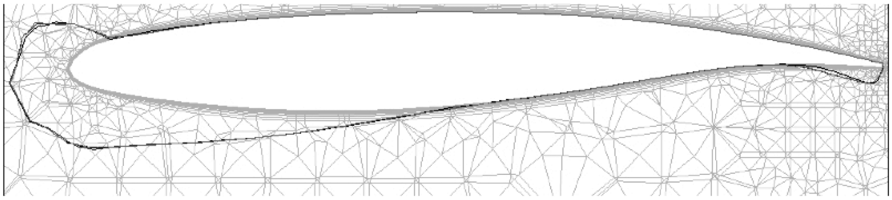

e) 98% span

Fig. 34 Iced wing at various span locations for the three different computations for AOA = 6 deg, $T = 261.5$.

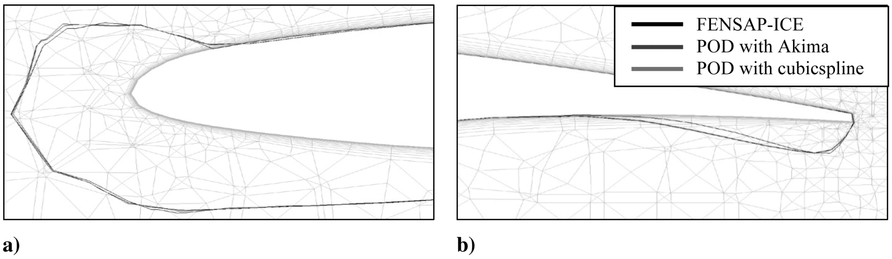

Fig. 35 **Comparison of the ice accretion around the a) leading and b) trailing edges at the 50% span for the three different computations for AOA = 6 deg, $T = 261.5$.**

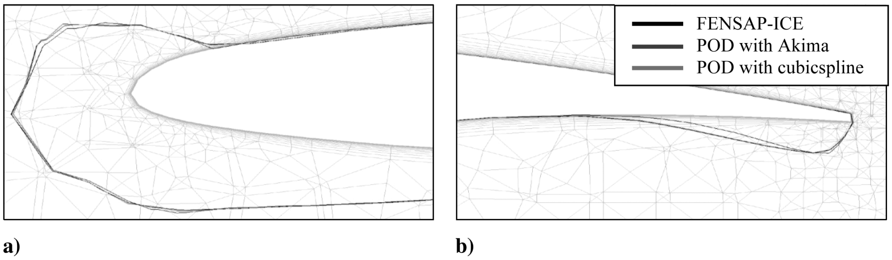

Fig. 36 **Comparison of the ice accretion around the a) leading and b) trailing edges at the 98% span for the three different computations for AOA = 6 deg, $T = 261.5$.**

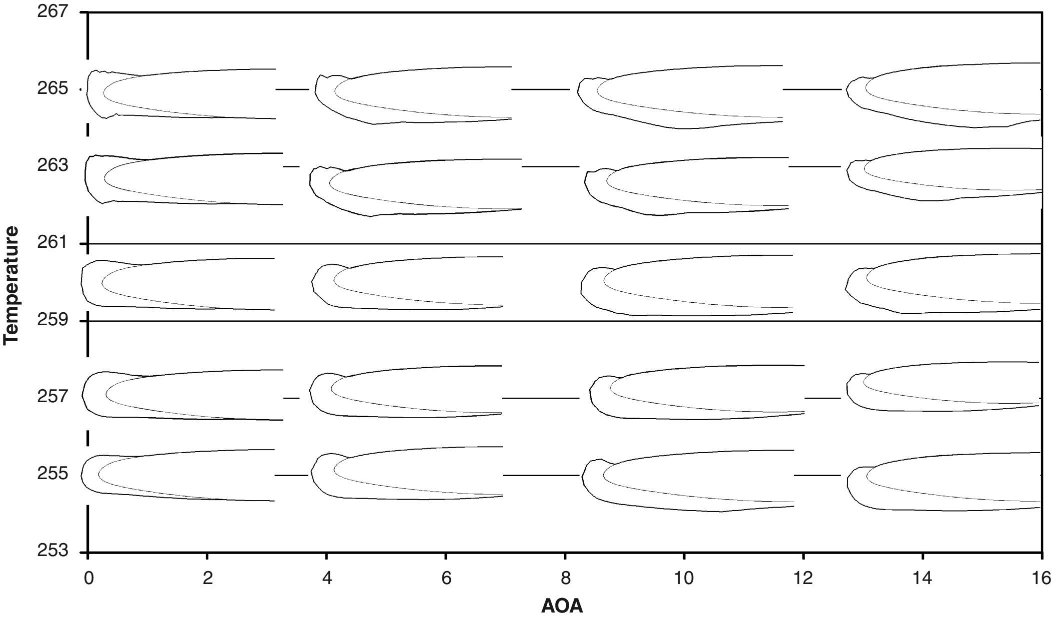

Fig. 37 **Complete map of ice shapes at position = 0.3 (y/span) by POD ranging from rime ice to glaze ice.**

References

[1] Shin, J., and Bond, T. H., "Results of an Icing Test on a NACA 0012 Airfoil in the NASA Icing Research Tunnel," NASA TM 105374, 1992.

[2] Habashi, W. G., Dompierre, J., Bourgault, Y., Fortin, M., and Vallet, M. G., "Certifiable Computational Fluid Dynamics Through Mesh Optimization, Special Issue on Credible Computational Fluid Dynamics Simulation," *AIAA Journal*, Vol. 36, No. 5, 1998, pp. 703–711.
doi:10.2514/2.458

[3] Bourgault, Y., Boutanios, Y., and Habashi, W. G., "3D Eulerian Droplets Impingement Using FENSAP-ICE, Part I: Model, Algorithms and Validation," *Journal of Aircraft*, Vol. 37, No. 1, 2000, pp. 95–103.
doi:10.2514/2.2566

[4] Beaugendre, H., Morency, F., and Habashi, W. G., "ICE3D, FENSAP-ICE's 3D In-Flight Ice Accretion Module," *Journal of Aircraft*, Vol. 40, No. 2, 2003, pp. 239–247.
doi:10.2514/2.3113

[5] Spalart, P. R., and Allmaras, S. R., "A One-Equation Turbulence Model for Aerodynamic Flows," AIAA Paper 92-0439, 1992.

[6] Gresho, P. M., Lee, R. L., Sani, R. L., Maslanik, M. K., and Eaton, B. E., "The Consistent Galerkin FEM for Computing Derived Boundary Quantities in Thermal and/or Fluid Problems," *International Journal for Numerical Methods in Fluids*, Vol. 7, 1987, pp. 371–394.
doi:10.1002/fld.1650070406

[7] Clift, R., Grace, J. R., and Weber, M. E., *Bubbles, Drops and Particles*, Academic Press, New York, 1978.

[8] Hughes, T. J. R., and Brooks, A., "A Theoretical Framework for Petrov–Galerkin Methods with Discontinuous Weighting Functions: Application to the Streamline-Upwind Procedure," *Finite Elements in Fluids*, Vol. 4, Wiley, New York, 1982, Chap. 3.

[9] Messinger, B. L., "Equilibrium Temperature of an Unheated Icing Surface as a Function of Air Speed," *Journal of the Aeronautical Sciences*, Vol. 20, No. 1, 1953, pp. 29–42.

[10] Morency, F., Tezok, F., and Paraschivoiu, I., "Anti-Icing System Simulation Using CANICE," *Journal of Aircraft*, Vol. 36, 1999, pp. 999–1006.
doi:10.2514/2.2541

[11] Hedde, T., "Modélisation Tridimensionnelle des Dépôts de Givre sur les Voilures d'Aéronefs," Ph.D. Dissertation, Univ. Blaise-Pascal, Clermont-Ferrand, France, 1992.

[12] Ruff, G. A., and Berkowitz, M., "Users Manual for the NASA Lewis Ice Accretion Prediction Code (LEWICE)," NASA CR 185129, 1990.

[13] Tran, P., Brahimi, M. T., and Paraschivoiu, I., "Ice Accretion on Aircraft Wings with Thermodynamic Effects," AIAA Paper 94-0605, 1994.

[14] Loéve, M., *Probability Theory*, Van Nostrand, New York, 1967, pp. 166–178.

[15] Cazemier, W., Verstappen, R. W. C. P., and Veldman, A. E. P., "Proper Orthogonal Decomposition and Low-Dimensional Models for Driven Cavity," *Physics of Fluids*, Vol. 10, No. 7, 1998, pp. 1685–1699.
doi:10.1063/1.869686

[16] Bui-Thanh, T., Damodaran, M., and K. W., "Proper Orthogonal Decomposition and Low-Dimensional Models for Driven Cavity," AIAA Paper 2003-4213, 2003.

[17] Epureanu, B. I., Dowell, E. H., and Hall, K., "A Parametric Analysis of Reduced Order Models of Potential Flows in Turbomachinery Using Proper Orthogonal Decomposition," ASME Paper 2001-GT-0434, 2001.

[18] Sirovich, L., "Turbulence and the Dynamics of Coherent Structures: Parts I, II, and III," *Quarterly of Applied Mathematics*, Vol. 45, 1987, pp. 561–590.

[19] Holmes, P., Lumley, J., and Berkooz, G., *Turbulence, Coherent Structures, Dynamical Systems and Symmetry*, Cambridge Univ. Press, Cambridge, England, UK, 1996.

[20] Akima, H., "A New Method of Interpolation and Smooth Curve Fitting Based on Local Procedure," *Journal of the Association for Computing Machinery*, Vol. 17, 1970, pp. 589–602.
doi:10.1145/321607.321609

[21] Akima, H., "A Method of Bivariate Interpolation and Smooth Surface Fitting for Irregularly Distributed Data Points," *ACM Transactions on Mathematical Software*, Vol. 4, No. 2, 1978, pp. 148–159.
doi:10.1145/355780.355786

[22] K. L., Brodersen, O., Rakowitz, M., Vassberg, J., Wahls, R., and Morrison, J., "Summary of Data from the Second AIAA CFD Drag Prediction Workshop," AIAA Paper 2004-555, 2004.